J Mater Sci: Mater Electron (2023) 34:713

The investigation of structural, surface topography, and optical behaviors of Al-doped ZnO thin films with annealing temperature deposited by RF magnetron sputtering

Mahdiyeh Shiravand[1], Nader Ghobadi[1,*] , and Ebrahim Gholami Hatam[1]

[1] *Department of Physics, Faculty of Sciences, Malayer University, Malayer, Iran*

Received: 1 December 2022
Accepted: 15 February 2023
Published online:
8 March 2023

© The Author(s), under exclusive licence to Springer Science+Business Media, LLC, part of Springer Nature 2023

ABSTRACT

Aluminum-doped Zinc oxide (AZO) thin films were sputtered on glass substrates, by RF magnetron sputtering method. The prepared films are annealed in the electrical furnace at various temperatures such as room temperature, 350, and 450 °C. The influence of annealing temperature on the structural, surface topography, and optical properties was evaluated. The structural characteristics of AZO films were investigated by XRD and FESEM analyses. The optical values were determined by ultraviolet–visible spectroscopy. The band gap energy was measured by the DITM method without the need of film thickness and any presumption about transition natural. The type of optical transition, refractive index, and dielectric constant at the absorption edge and their relationship with band gap energy were calculated by this method. The other optical quantities including Urbach energy, the strength of electron–phonon interaction, the penetration depth, optical density, dissipation factor, lattice dielectric constant, and optical conductivity of the films were also reported. The surface topography of the samples was measured by AFM technique and its relationship was investigated with Urbach energy. The highest optical transmittance was observed in the visible range for films annealed at 350 °C which make them applicable for optoelectronic devices.

1 Introduction

The zinc oxide thin films (ZnO) are classified in the II–VI compound semiconductors material and are composed of hexagonal wurtzite crystal structure with $a = 3.25$ Å and $c = 5.12$ Å. In its structure band, Zn atom is tetrahedrally coordinated to four O atoms in a way that the Zn d-electrons hybridize with the O p-electron. Hence, shells occupied by Zn atom alternate with shells occupied by O atom and utilizes the ZnO as the transparent conductive oxide (TCO) in thin films. The interesting features of ZnO are wide

Address correspondence to E-mail: n.ghobadi@malayeru.ac.ir

https://doi.org/10.1007/s10854-023-10110-9

band gap (3.35–3.37 eV) and large exciton binding energy of 60 meV which allow a lower threshold for optical pumping at room temperature (RT). High transmittance property in the visible region, piezoelectric properties, high coupling factor, and ferromagnetism features have attraction for studying [1–11]. Besides, to the privilege of undoped ZnO films owing to high resistivity, instability, and low conductivity it is preferred doping them by the small amount of the elements of group III such as Al, Ba, Ga, and In for decreasing the resistivity and improving the electrical properties [12]. Among these TCO materials, the dopant of Aluminum on ZnO (AZO) thin films semiconductors is preferred owing to low resistivity of 10^{-4} Ω cm, high optical transparency in the visible region, cost-effective fabrication, non-toxic nature, easy to prepare, high electrical conductivity, chemical, mechanical, and thermal stability, direct wide band gap, and lowering the lattice strain by doping. AZO thin films have been extensively used for some devices, such as gas sensors, diodes, solar cells, displays, electrochromic devices, transparent electrode application, catalysts, UV laser, and transistors [13–15].

The methods of preparing thin films can be divided into chemical and physical methods. The physical methods include the thermal evaporation, the ion coating, direct current (DC) magnetron sputtering, radio frequency (RF) magnetron sputtering, and high power impulse (PVD) magnetron sputtering [16–18]. The chemical methods include deposition methods by electrolysis in the cathode, chemical vapor deposition (CVD), chemical bath deposition (CBD), sol–gel, and etc. [19–22]. In the present work, AZO thin film was sputtered by RF magnetron sputtering method due to its flexibility and ability to deposit films under a vacuum, control over the composition, stoichiometry, and good adhesion of films. To explore these capabilities, the structural, optical properties, and surface topography of AZO thin films with changing of annealing temperature were investigated. For better accuracy and predicting the photochemical and photophysical behaviors of semiconductors, Derivation of ineffective thickness method (DITM) was employed to extract the optical band gap energy and the type of optical transitions in nanostructured semiconductors. Through this approach, it is shown that the optical band gap is independent from thickness measuring and only requires the measurement of the absorbance spectrum of the products. Numerical factors for sample surfaces as used in material surface drawings are the means of communication between fabrication and functional performance. These factors are not only used as a criterion for production and surface parameter description but also to predict physical properties particularly in the case of 3D factors [23–26].

2 Experimental details

AZO thin film was sputtered by RF magnetron sputtering process where a disk of AZO with purity of 99.9% and a diameter of 100 mm was utilized as cathode. Before the sputtering process, the glass substrate was thoroughly cleaned in an ultrasonic bath with acetone and ethyl alcohol for 20 min to remove the particles attached to the surfaces. Then it was washed in deionized water and was dried in hot air and high pressure. The substrates were placed in the chamber vacuumed to a base pressure of 2.8×10^{-5} mbar prior to deposition. The pressure was enhanced to 2.3×10^{-2} mbar with argon gas with a purity of 99.9%. The AZO films were prepared with a RF power of 100 W, deposition time of 3 h, and thicknesses of 720 nm. The prepared films were annealed at RT and 350–450 °C in an electrical furnace for 1 h.

The absorption and transmittance were evaluated by an UltraViolet–Visible double-beam spectrophotometer (PerkinElmer, Lambda 25-USA), the X-ray diffraction (XRD) patterns were measured by diffractometer (Unisantis-XMD-300, Cu K_{α}, Germany), the microstructure image of the field emission scanning electron microscopy (FESEM) was captured by (Tscan, Mira lll, Czech Republic), surface topography was investigated by an atomic force microscopy (AFM) (Tscan, Mira lll, Czech Republic), annealing temperatures were adjusted by Bruker, Icon, USA and electrical furnace from AZAR furnaces FIL 1250, Iran was used.

3 Investigation the crystalline phases

Figure 1 shows the XRD spectra of AZO thin films at RT and with changing the annealing temperature from 350 to 450 °C. The patterns of XRD reveal diffraction peaks at 100, 002, 101, and 110 planes that

resembles to wurtzite hexagonal ZnO crystal. The Al_2O_3 phase was not detected because of the Al atoms replacement into the hexagonal lattice of Zn. In other words, Al atoms are separated into the non-crystalline region in the grain boundary. To obtain the detailed structural data, the size of nanocrystallite and lattice strain are calculated from the Williamson–Hall equation:

$$\beta \cos \theta_{hkl} = \frac{k\lambda}{D} + 4\varepsilon \sin \theta_{hkl}, \quad (1)$$

where k is the particle shape factor (0.9), λ stands for the K_α X-ray wavelength (1.5405 Å), β is the line broadening at half the maximum intensity (FWHM), θ is the Bragg angle of the diffraction peak and D is the size of nanocrystallites. The slope and vertical axis intercept of the plots of β cos (θ_{hkl}) versus 4 sin(θ_{hkl}) gives the lattice strain (ε^{W-H}) and the size of nanocrystallites (D^{W-H}) [30]. In Fig. 2, the size of nanocrystallites and the lattice strain have been calculated from the linear part of the obtained points for the crystal planes of 100, 002, 101, and 110. The size of nanocrystallites was increased with the increase of the annealing temperature (Table 1). One reason is that the surface mobility of the atoms on the substrate increases and they are placed in their special positions in the crystal lattice. The other reason is that with increasing the annealing temperature from 350 to 450 °C, the lattice strain has decreased due to the reduction of defects which is in agreement with results of Zak et al. [27].

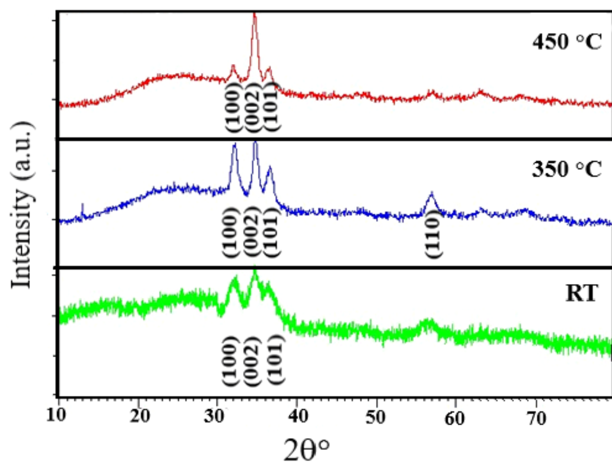

Fig. 1 XRD pattern of AZO thin film at RT and with the change of annealing temperature from 350 to 450 °C

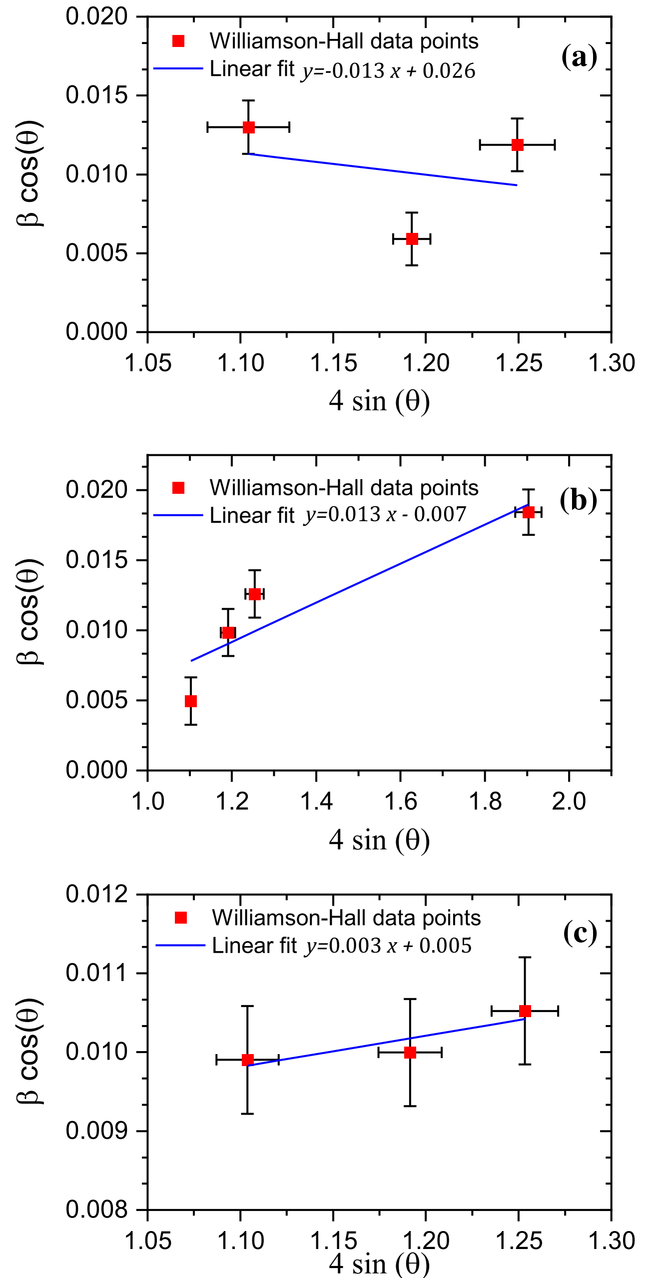

Fig. 2 Williamson–Hall diagram for AZO film, sputtered at **a** RT, **b** 350 °C, and **c** 450 °C; dashed line is the best linear fit from the least-square method

3.1 Investigating the surface morphology of AZO thin film

The surface morphology of the film plays an important role in investigating the change of various properties of thin metal oxide films. FESEM analysis was used to investigate the surface morphology and growth of nanocrystallites and to estimate the size of

Table 1 Analysis of XRD parameters of AZO thin film at different temperatures of RT, 350, and 450 °C by Williamson–Hall method

Annealing Temperature	Miller indices	Peak position ($2\theta°$)	FWHM (β_{hkl} °)	$D^{W–H}$(nm)	$\varepsilon^{W–H}$
RT	100	32.0535	0.7747	5.27	0.013
	002	34.6849	0.3542		
	101	36.3977	0.7160		
350 °C	100	31.9966	0.2952	19.58	0.013
	002	34.6333	0.5904		
	101	36.5328	0.7872		
	110	56.8205	1.2000		
450 °C	100	32.0396	0.5904	27.42	0.003
	002	34.6608	0.6000		
	101	36.5218	0.6350		

nanocrystallites on the surface of AZO thin films at various temperatures. The FESEM images (Fig. 3) confirm that the formed nanostructured phase of AZO films and the average nanocrystallites sizes were, respectively, 36.47, 79.28, and 128.68 nm at RT, 350, and 450 °C. The average nanocrystallite size increases with increasing the annealing temperature. This is in consistence with the XRD measurements (Table 1). To ensure the composition of the prepared sample elements a typical energy-dispersive X-ray spectroscopy (EDS) analysis was performed for sample annealed at 450 °C. The EDS spectrum of the thin film (Fig. 4) confirms that AZO is composed of Zn (82% wt), O (16% wt), and Al (2% wt) elements. We concluded that the small quantity of dopant (Aluminum) element is successfully incorporated and substituted into ZnO lattice without additional impurities.

3.2 Investigating the surface topography of the AZO thin film

Characterization of the surface topography of AZO thin film was obtained by AFM device in non-contact mode. Two-dimensional images of the surface topography of AZO thin films at RT, 350, and 450 °C are presented at Fig. 5. The AFM images show that the surface of the film is rough at RT where grains and intergranular valleys appear and are smooth for the AZO film annealed at 450 °C where the valleys of the surface are filled and the films become smoother. To quantitatively describe these behaviors the roughness parameters including root mean square roughness (S_q), the skewness parameter (S_{sk}), the kurtosis parameter (S_{ku}), and the roughness average (S_a) calculated from AFM images are given in Table 2. The roughness dispersion parameter of S_q, which characterizes the surface roughness, is obtained by squaring each height value in the dataset and then taking the square root of the mean, which was 22.44, 24.40, and 14.40 nm for the films annealed at RT, 350, and 450 °C annealing temperatures. The same behavior was observed for the average roughness parameter S_a. S_z, ($S_z = S_p + S_v$), average of the height difference between five highest peaks, and the five lowest valleys were calculated to be 186.5, 184.7, and 115.8 nm at RT, 350 and 450 °C, respectively. This parameter indicates that the AZO thin films became structurally more regular by increasing the annealing temperature and this behavior is consistent with similar studies [28–31].

4 Optical properties measurement

4.1 Optical transmittance and absorption spectrum of AZO film

The spectrum of optical transmittance was investigated by the ultraviolet–visible spectrometer in the wavelength range of 190 to 1100 nm for AZO thin films at RT, 350, and 450 °C (Fig. 6). The AZO thin film at RT shows the highest optical transmittance. As the thickness of the films increases the optical transmittance decreases in the visible region. The optical transmittance was measured 86.25, 84.30, and 81.70% in the visible region for thin films, respectively, when annealed at RT, 350, and 450 °C. In overall, the optical transmittance was less than 70% in the ultraviolet range and more than 80% in the visible range. From the optical absorption spectrum for AZO thin films (Fig. 7), the absorption edge shifts toward longer wavelengths (red shift) by uprising the annealing temperature for AZO from RT to 450 °C

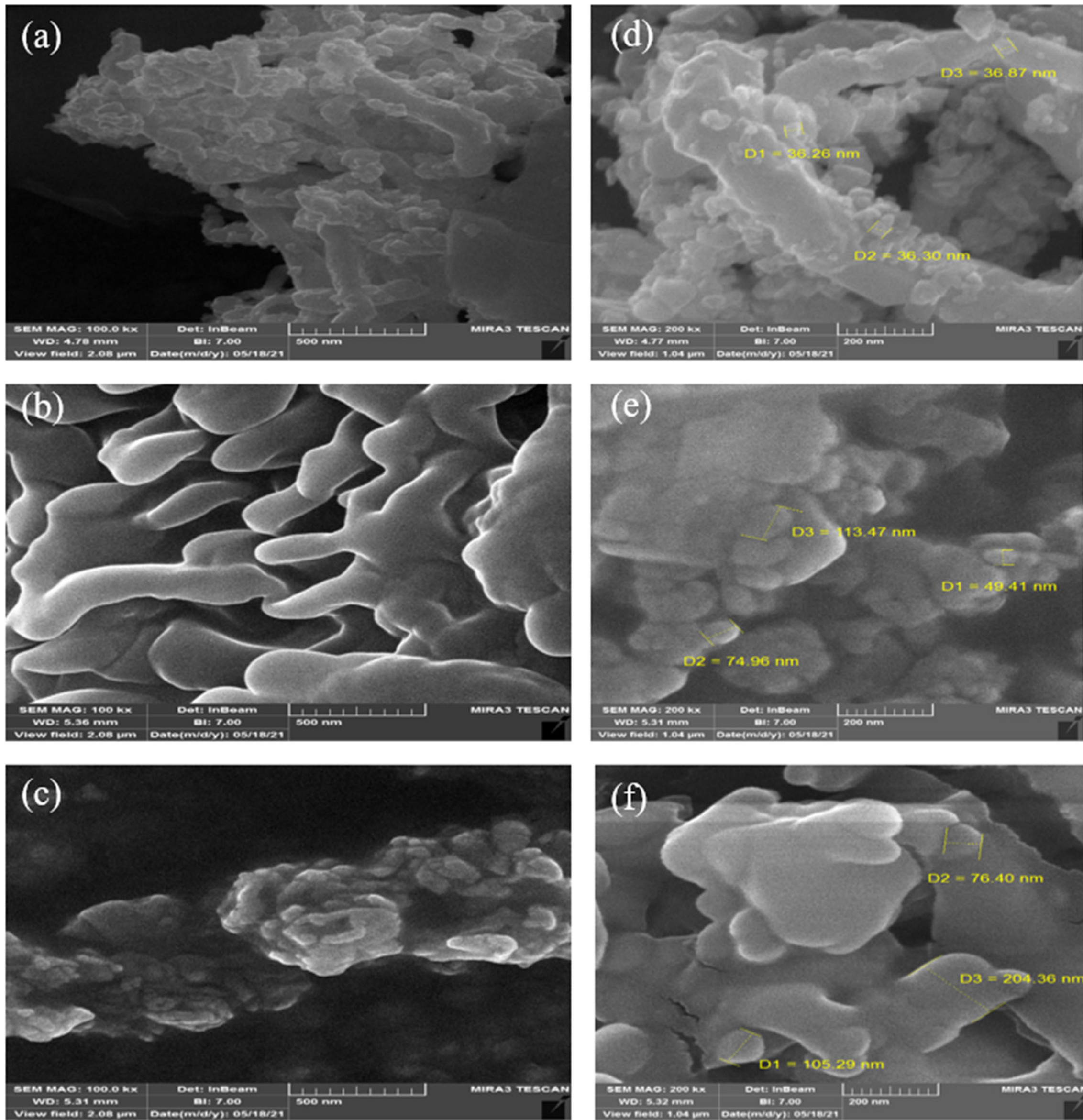

Fig. 3 The FESEM micrograph of AZO thin films annealed at **a** RT, **b** 350 °C, and **c** 450 °C with magnification of 500 nm and **d**, **e**, and **f** the same temperature with magnification of 200 nm

which indicates the formation of AZO films semiconductor [32–35].

4.2 The band gap energy and the optical transition

The optical band gap energy is determined by the DITM method starting from the following equation [26].

$$\frac{d\{Ln[A(v)E)\}}{d(E)} = \frac{m}{E - E_{gap}}, \tag{2}$$

where A, E, and E_{gap} are optical absorption, incident photon energy, and band gap energy, respectively, and the value of m depends on the nature of the optical transition. If the graphs of $\frac{d\{\mathrm{Ln}[A(v)E)\}}{d(E)}$ versus E are drawn, there would be a discontinuity at $E = E_{\mathrm{gap}}$ indicating the band gap energy. Figure 8 shows the plot of DITM method for calculating the band gap energy at RT and by increasing the annealing temperature from 350 to 450 °C, the band gap energy was decreased from 3.32 to 3.22 eV. One of the reasons for this decrease in the band gap energy is the increase in the size of nanocrystallites in

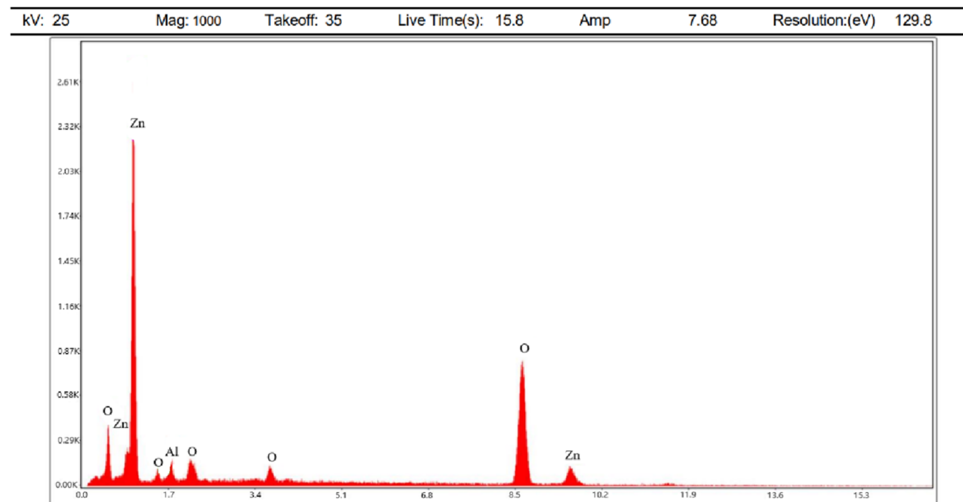

Fig. 4 The EDX spectrum of AZO prepared at 450 °C

a way that when the size of the nanocrystallites increases there are more atoms and more atomic orbitals to overlap. Therefore, the number of molecular orbitals, both bonding and non-bonding, increases and the distance between the two bands decreases in accordance to the band gap energy reduction. In turn, the decrease of band gap energy can be due to the increase of the fundamental absorption edge toward longer wavelengths.

Using the values of band gap energy, the transition index can be measured from the slope of the linear part of Ln (AE), in terms of Ln ($E-E_{gap}$) (Fig. 9). The measured values of m near to ½ is representative of the direct allowed transition for the AZO film (The transition index, m, is also given in Table 3).

4.3 Urbach energy, steepness, and the strength of electron–phonon interaction parameters

Continuing along the absorption curve and close to the edge of the optical band gap, there is an exponential section called the Urbach tail that is due to the absence of long-range order. The Urbach energy is calculated from the following equation [26]:

$$LnA(v) = LnA_0 + {}^{hv}/_{E_{tail}}, \tag{3}$$

where A_0 is a constant, hv is the incident photon energy, and E_{tail} is the Urbach tail energy that can be obtained by plotting Ln $A(v)$ versus incident photon energy (Fig. 10). The calculated values of Urbach energy decreased by increasing the annealing temperature. AFM results confirm these measurements, as the S_z parameter (which shows the distance between the peak and the valley) was decreased at RT, 350, and 450 °C. In fact, by increasing the annealing temperature, the AZO film becomes more orderly. The other reason for the reduction of Urbach energy is due to the increase in the thickness of the films, as the width of the localized state tail was decreased when the thickness of the film was increased.

By calculating the Urbach energy, the steepness (σ) parameter, which describes the broadening of optical absorption edges due to electron–phonon or exciton–phonon interactions, can also be calculated from the following equation [32, 36]:

$$\sigma = \frac{k_B T}{E_{tail}}, \tag{4}$$

where K_B and T are Boltzmann's constant and Kelvin's absolute temperature. The strength of electron–phonon interaction is also related to the steepness parameter via

$$E_{el-ph} = \frac{2}{3\sigma}. \tag{5}$$

The decrease of localized states and the decrease of defects and vacancies with increasing the annealing temperature has led to the increase of the σ parameter and the decrease of the strength of the electron–phonon interaction (Table 3).

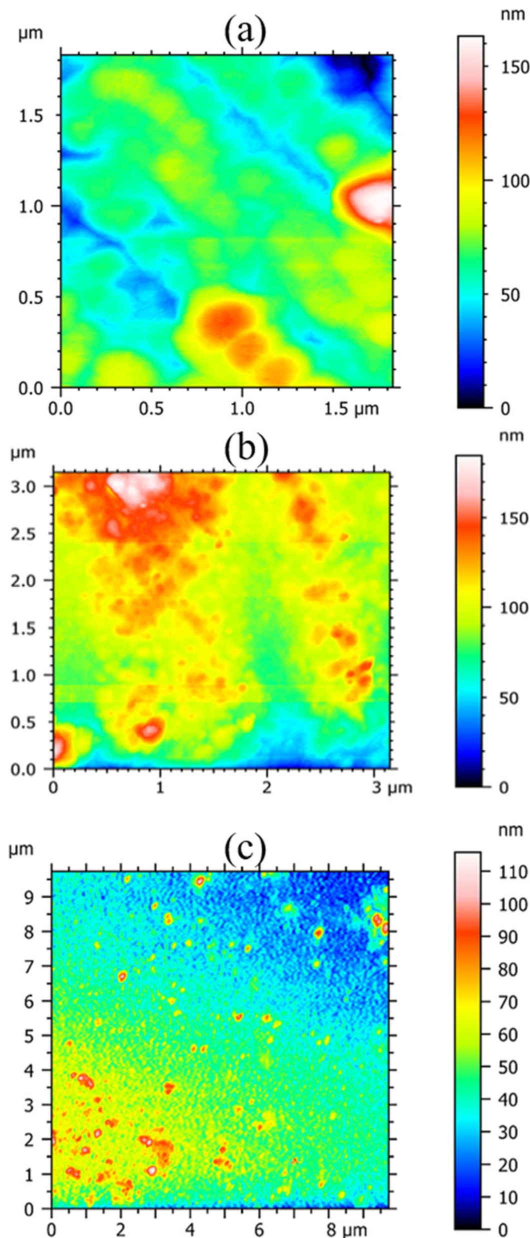

Fig. 5 AFM images of AZO thin films annealed at **a** RT, **b** 350 °C, and **c** 450 °C

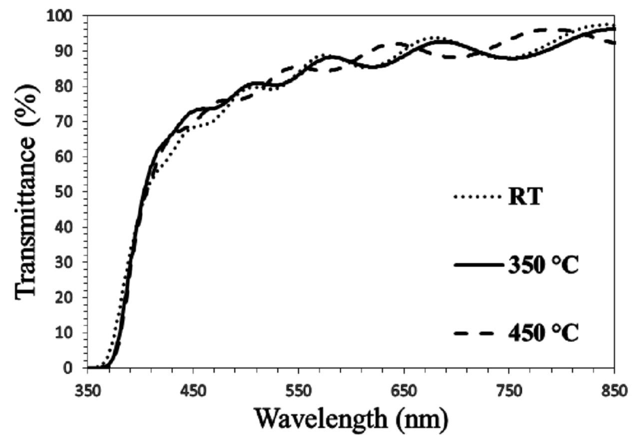

Fig. 6 The spectrum of optical transmittance of AZO thin film annealed at RT, 350, and 450 °C

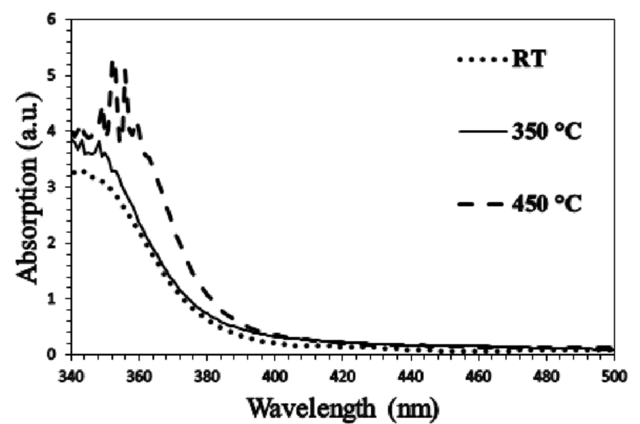

Fig. 7 The spectrum of optical absorption of AZO thin film prepared at RT, 350, and 450 °C

5 Penetration depth and optical density of AZO thin films

One of the important parameters in determining the optical properties of materials is the penetration depth, which is equal to the inverse of the absorption coefficient and is calculated from the following equation [36]:

Table 2 Topography parameters of the surfaces of AZO thin films, at RT, 350, and 450 °C

Annealing temperature (°C)	S_q (nm)	S_{sk}	S_{ku}	S_p (nm)	S_v (nm)	S_z (nm)	S_a (nm)
RT	22.44	0.8646	6.771	110.70	75.84	186.5	16.26
350	24.40	0.0468	3.879	85.26	99.48	184.7	18.28
450	14.40	0.5147	3.672	72.38	43.46	115.8	11.12

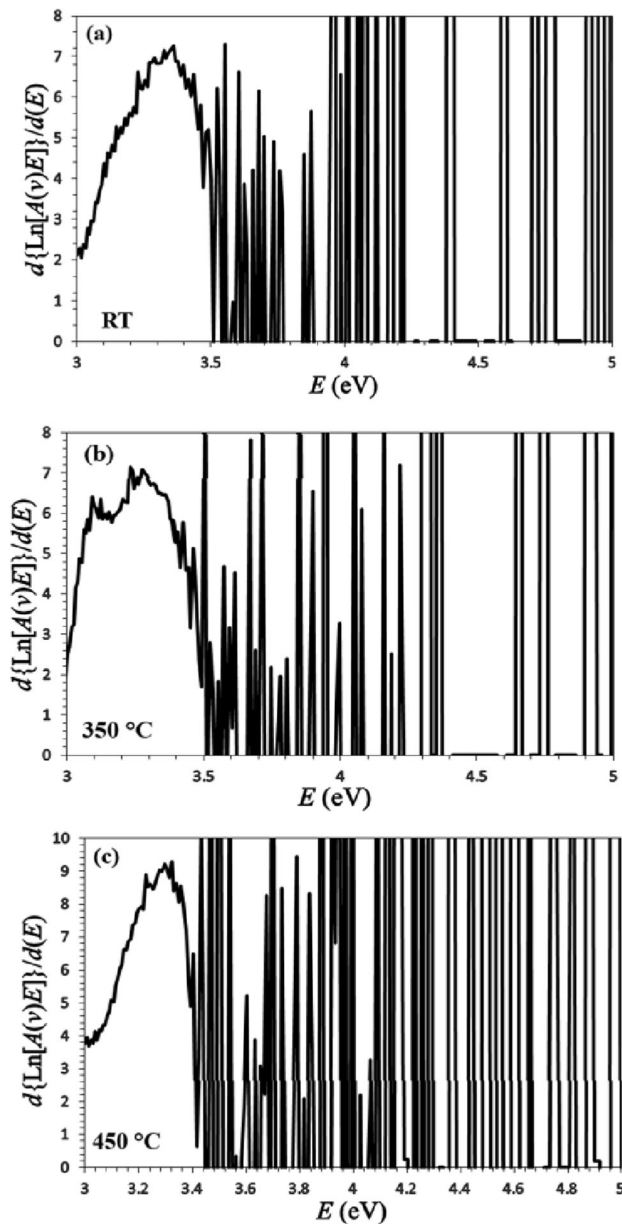

Fig. 8 DITM plots of AZO thin films at three different annealing temperatures of **a** RT, **b** 350, and **c** 450 °C

$$\chi = \frac{1}{\alpha}. \tag{6}$$

Figure 11 shows the penetration depth of AZO thin film versus the incident photon wavelength at RT, 350, and 450 °C annealing temperatures. In visible wavelengths, the penetration depth is high, while it reaches its minimum value in ultraviolet wavelengths. In addition, the penetration depth reaches its lowest value at the wavelength of the absorption edge due to the strong interaction between the

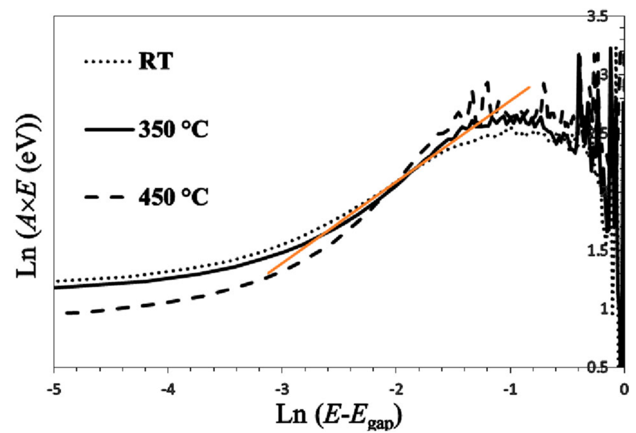

Fig. 9 Plot of Ln (AE), in terms of Ln (E-Egap) for deposited films at RT, 350, and 450 °C and a linear extrapolation is drawn for the film prepared at RT

conduction electrons and incident photons. This property of thin films is favorite for optical equipment application.

The optical density of films is a quantitative expression of the absorbed light by the material. The estimation of optical density is a common method for quantifying various parameters such as the concentration of films and variation in the film morphology that is calculated from this equation [37]:

$$D_{opt} = \alpha t, \tag{7}$$

where α is the absorption coefficient and t is the thickness of the films. Figure 12 shows the plot of optical density of the AZO films versus the incident photon energy. The optical density of the films increases by the annealing temperature up to a constant energy of 3.1 eV and then from 3.1 to 3.5 eV has a sharp slope which enables the prediction of the band gap energy between 3.1 and 3.5 eV for the films. In addition, with increasing annealing temperature, the thickness of the film was also increased, so the optical density of the film was decreased.

5.1 Dielectric constants, dissipation factor, lattice dielectric constant, and optical conductivity of the films

Optical features including refractive index (n) and extinction coefficient (k) play an essential part in TCO film optical properties investigations. The refractive index (n) is defined by

Table 3 The optical values calculated for AZO thin film at RT, 350, and 450 °C annealing temperatures

Annealing temperature (°C)	T (%)	E_{gap} (DITM method) (eV)	(m)	E_{tail} (eV)	σ(10^{-2})	$E_{el\text{-}ph}$
RT	86.25	3.32	0.701	0.153	16.896	3.94
350	84.30	3.30	0.650	0.138	18.730	3.55
450	81.70	3.22	0.831	0.119	21.720	3.06

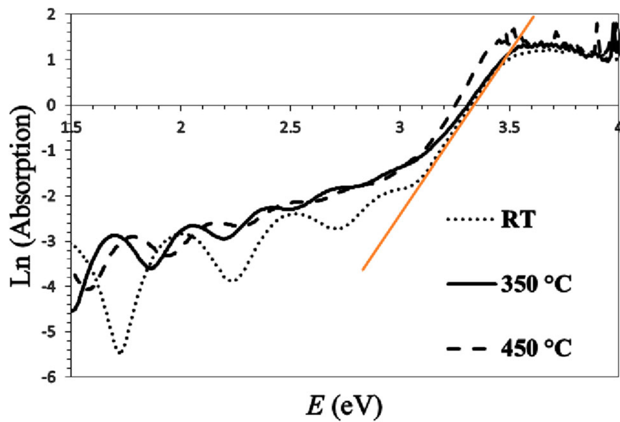

Fig. 10 Plot of Ln A, in terms of incident photon energy for deposited AZO films at RT, 350, and 450 °C and a linear extrapolation is drawn for the film prepared at RT

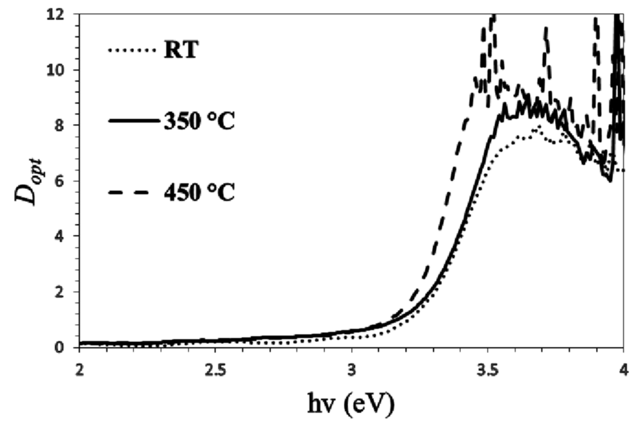

Fig. 12 The optical density of the AZO films according to the incident photon energy at RT, 350, and 450 °C

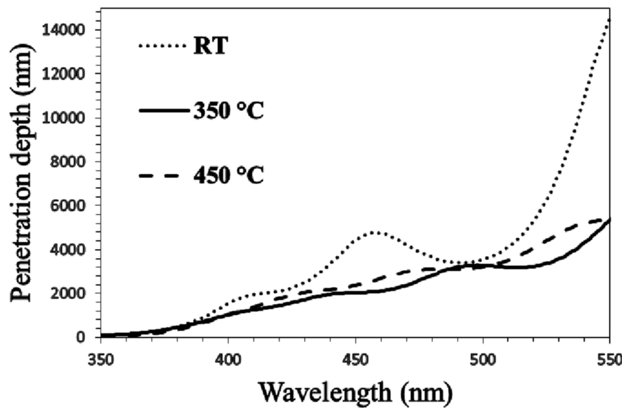

Fig. 11 Penetration depth diagram according to the incident photon wavelength at RT, 350, and 450 °C

$$n = \frac{(1+R)}{(1-R)} + \sqrt{\frac{4R}{(1-R)^2} - k^2}, \tag{8}$$

where R is the reflectance and k is the extinction coefficient measurements. Figure 13 shows the graph of the refractive index in terms of wavelength. The refractive index decreases with a constant slope at longer wavelengths and shorter wavelengths close to the absorption region. The refractive index has its maximum value for AZO film annealed at 450 °C (Table 4) due to the strong interaction of incident photons and conduction electrons. The extinction coefficient (k) measurement can be calculated from the below equation:

$$k = \frac{\alpha(\lambda)\lambda}{4\pi}. \tag{9}$$

Figure 14 shows the change of the extinction coefficient in terms of the wavelength, which was

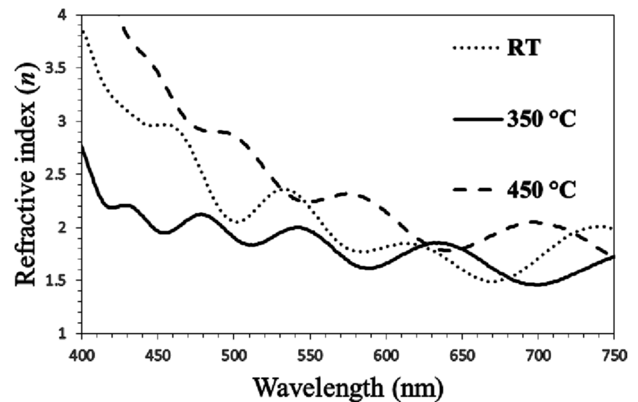

Fig. 13 The graph of the refractive index in terms of the wavelength at RT, 350, and 450 °C annealing temperatures

decreased by increasing the annealing temperature due to the improvement of the crystallinity, smooth surface, reduction of defects, and high transmittance of the films. The extinction coefficient calculated near the absorption edge show a higher value, in agreement with references [32, 38], where the interaction between conduction electrons and incident photons is high. The results are summarized in Table 4.

The dielectric constant is an inherent and fundamental property of materials. The real part of the dielectric constant, ε_1, shows the material's ability to store electrical energy, is related to polarization, and expresses how much the speed of light will slow down in the material. The imaginary part of the dielectric constant, ε_2, is the material's energy loss of the electric field and how the dielectric material absorbs energy from an electric field which are expressed by [32, 38]

$$\varepsilon_1 = n^2 - k^2, \tag{10}$$

$$\varepsilon_2 = 2nk. \tag{11}$$

Figure 15 and 16 show the real and imaginary parts of dielectric constant diagrams in terms of incident photon energy. The calculated constant diagrams show a higher value near the absorption edge (higher energies) due to strong interaction between conduction electrons and incident photons. The calculated values are low and can be related to the high optical transmittance of the prepared films. In these films, the real dielectric constant behaves like the refractive index. The calculated real dielectric constants are higher than imaginary values. The polarization property of the films is more in the ultraviolet region and this can be used in short wavelengths to create polarized rays. The data are given in Table 4.

The dissipation factor (tan δ) is a physical optical quantity that depends on the real and imaginary part of dielectric constants. Measuring the power loss rate of a mechanical mode is like an oscillation in a dissipative system and represents the loss of electrical energy in the form of heat energy and is expressed by [39]

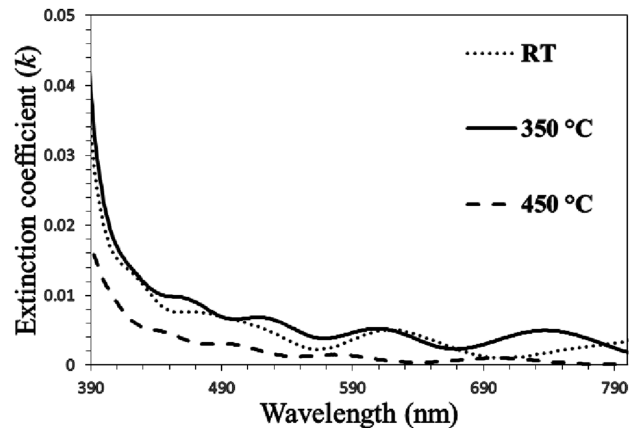

Fig. 14 The graph of extinction coefficient in terms of the wavelength at RT, 350, and 450 °C annealing temperatures

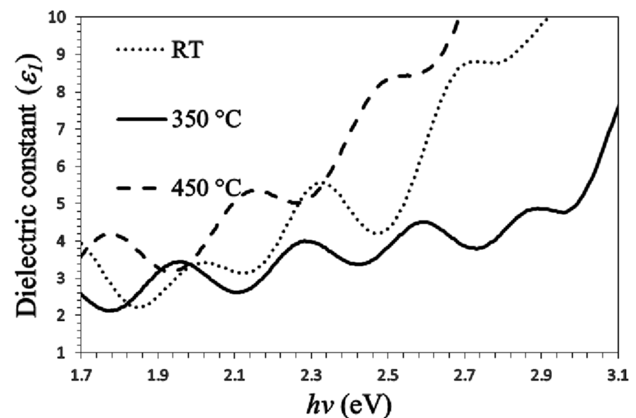

Fig. 15 The real dielectric constant diagram in terms of incident photon energy at RT, 350, and 450 °C annealing temperatures

$$tan\delta = \frac{\varepsilon_2}{\varepsilon_1}. \tag{12}$$

Figure 17 shows the dissipation factor graph in terms of incident photon energy, which has decreased with increasing annealing temperature. The lowest value of the dissipation factor has been calculated for the AZO film annealed at 450 °C. The data for other temperatures are given in Table 4.

The relationship between the lattice dielectric constant (ε_L) and the refractive index (n) is described by [32]

Table 4 Additional calculated optical values for AZO thin film at RT, 350, and 450 °C annealing temperatures

Annealing temperature	n	k	ε_1	ε_2	tan δ
RT	1.9494	0.0074	3.9320	0.0321	0.0081
350 °C	1.8856	0.0067	3.6123	0.0269	0.0074
450 °C	2.6778	0.0025	8.0905	0.0178	0.0022

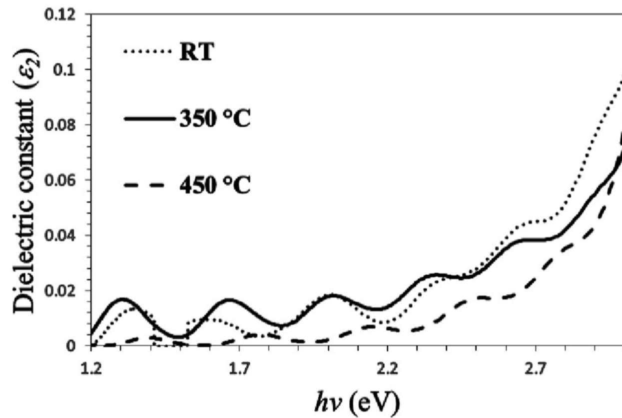

Fig. 16 The imaginary dielectric constant diagram in terms of incident photon energy at RT, 350, and 450 °C annealing temperature

$$\varepsilon_1 = n^2 - k^2 = \varepsilon_L - \frac{e^2 N}{4\pi^2 c^2 \varepsilon_0 m^*}\lambda^2, \quad (13)$$

where ε_1, e, c, N/m^*, ε_L, and ε_0 are the real part of the dielectric constant, the electron charge, the speed of light, the ratio of the free charge carrier concentration to the effective mass, the lattice dielectric constant, and the permittivity of free space. The slope and vertical axis intercept of the plots of ε_1 versus λ^2 give the N/m^* and ε_L, respectively. From Fig. 18, by drawing ε_1, in terms of λ^2 and calculating the linear part, N/m^* and the lattice dielectric constant were calculated. The highest value of N/m^* for the AZO thin films was observed at 450 °C annealing temperature, which indicates the reduction of localized states and the transfer of the percentage of localized charge carriers to the percentage of free charge carriers. Hence, by increasing the annealing temperature, the size of the nanocrystallites increases and leads to an increase in the surface diffusion of the nanocrystallites and results in aluminum content reduction. In other words, the localized states are reduced and it causes the transfer of the percentage of localized charge carriers to percentage of free charge carriers and consequently N/m^* is increased. The more increase in annealing temperature results in the more lattice dielectric constant (Table 5).

The optical response of materials is generally studied in terms of optical conductivity which directly depends on the absorption coefficient and refractive index through this relation [39]:

$$\sigma_{opt} = \frac{\alpha n c}{4\pi}, \quad (14)$$

where α is the absorption coefficient, n is the refractive index, and c is the speed of light. Figure 19a shows the optical conductivity in terms of incident photon energy for AZO thin films at RT and 350 °C and Fig. 19b shows the optical conductivity for AZO film annealed at 450 °C. The optical conductivity of the films in the transparent region changes with a slight slope, while it increases in short wavelengths until it reaches its maximum value. The highest optical conductivity value has been observed for AZO thin film annealed at 450 °C due to the increase in the size of nanocrystallites. The optical conductivity increases exponentially for energies higher than 3 eV which relates to the obtained band gap energy value of the films and equals to the energy of electrons transferring to the conduction band. This property of films can be used in the construction of optical fibers for information transmission.

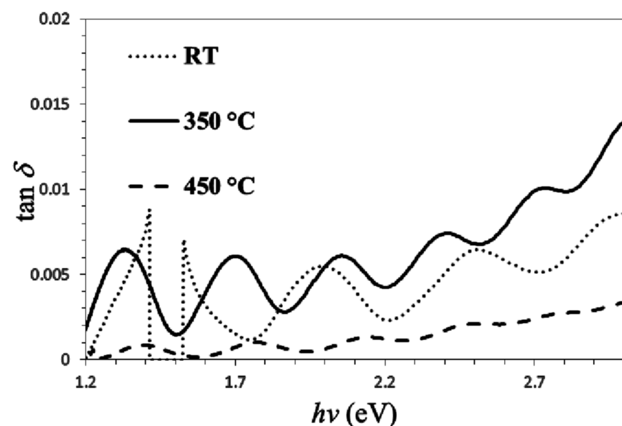

Fig. 17 Dissipation factor diagram according to incident photon energy at RT, 350, and 450 °C annealing temperatures

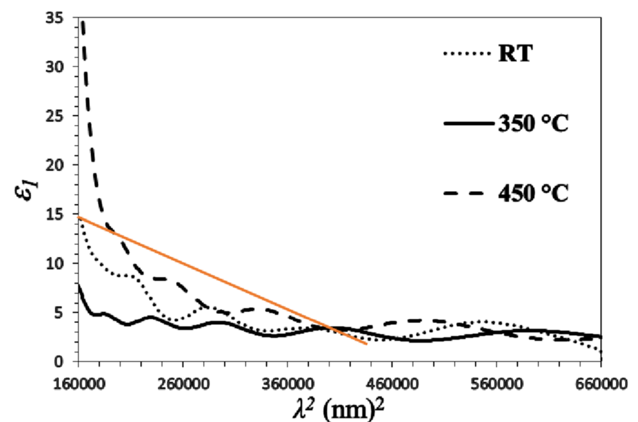

Fig. 18 Plot of ε1 in terms of λ2 for AZO thin film at RT, 350, and 450 °C annealing temperatures

Table 5 Additional optical values calculated for AZO thin film at RT, 350, and 450 °C annealing temperatures

Annealing temperature (°C)	N/m^* (10^{40} m^{-3} kg^{-1})	ε_L	$n_{\text{at the edge of absorption}}$	$\varepsilon_{\text{at the edge of absorption}}$
RT	1.3065	8.2968	2.31	5.35
350	1.4500	8.7400	2.32	5.38
450	6.1350	23.9780	2.34	5.47

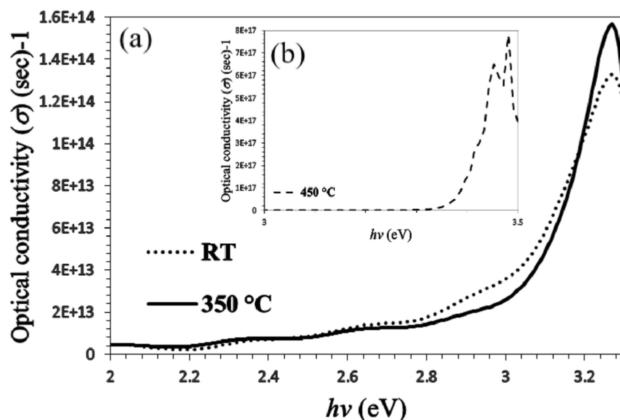

Fig. 19 The optical conductivity diagram according to incident photon energy at **a** RT, 350, and **b** 450 °C

6 Refractive index and dielectric constant at the absorption edge

Since the optical properties such as refractive index and band gap energy play an important part in thin films and for further analysis of optical data the values of refractive index and dielectric constant (the ratio of the permittivity of material to the permittivity of free space) at the absorption edge are calculated according to Dimitrov and Sakaa equation [35, 40]:

$$\frac{n^2-1}{n^2+2}=1-\left(\frac{E_g}{20}\right)^{\frac{1}{2}}, \quad (15)$$

$$\varepsilon=n^2. \quad (16)$$

The refractive index and dielectric constant at the absorption edge were increased by increasing the annealing temperature from RT to 450 °C (Table 5).

7 Conclusion

Through this study we have discussed the effect of annealing temperature on the structural, surface topography parameters, and optical properties of Al-doped ZnO thin films synthesized by RF magnetron sputtering technique. At first a typical EDS analysis confirmed the existence of Al in ZnO with no additional elements. From the XRD measurements it was concluded that the crystal quality of the films depends on the annealing temperature and from the Williamson–Hall method it was revealed that the lattice strain and the size of nanocrystallites increases by uprising the annealing temperature as these results were in agreement with FESEM analyze and optical conductivity. The band gap energy and transition index were determined by recent introduced method of DITM method and the calculated results indicate that AZO film is a semiconductor with the direct allowed transition. In addition, from the surface topography parameters it was deduced that by increasing the annealing temperature the surfaces become smooth and the distance between peaks and valley decreases in a way that the AZO annealed at 450 °C has the lowest disorder. AZO thin films show a high optical transmittance in the visible region, so these films can be used in TCO materials which makes them a good candidate for optoelectronic devices.

Author contributions

Not applicable.

Funding

Not applicable.

Data availability

Not applicable.

Code availability

Not applicable.

Declarations

Conflict of interest The authors declare that they have no known competing financial interests or personal relationships that could have appeared to influence the work reported in this paper.

Ethical approval Not applicable.

Consent to participate Not applicable.

Consent for publication Not applicable.

References

1. T.K. Subramanyam, P. Goutham, S.P. Kumar et al., Optimization of sputtered AZO thin films for device application. Mater. Today: Proc. **5**(4), 10851–10859 (2018)
2. K.E. Lee, M. Wang, E.J. Kim et al., Structural, electrical and optical properties of sol–gel AZO thin films. Curr. Appl. Phys. **9**(3), 683–687 (2009)
3. N. Navya, K.K. Ribin, K. Naseema, Structural, optical and morphological studies of SILAR grown ZnO thin film and double coated CBD grown ZnO thin film. J. Phys. **1706**(1), 012022 (2020)
4. S. Pat, R. Mohammadigharehbagh, S. Özen et al., The Al doping effect on the surface, optical, electrical and nanomechanical properties of the ZnO and AZO thin films prepared by RF sputtering technique. Vacuum **141**, 210–215 (2017)
5. K. Jang, H. Park, S. Jung et al., Optical and electrical properties of 2 wt.% Al2O3-doped ZnO films and characteristics of Al-doped ZnO thin-film transistors with ultra-thin gate insulators. Thin Solid Films **518**(10), 2808–2811 (2010)
6. S. Rahmane, M.A. Djouadi, M.S. Aida et al., Power and pressure effects upon magnetron sputtered aluminum doped ZnO films properties. Thin Solid Films **519**(1), 5–10 (2010)
7. K. Samanta, P. Bhattacharya, R.S. Katiyar, Raman scattering studies of p-type Sb-doped ZnO thin films. J. Appl. Phys. **108**(11), 113501 (2010)
8. K. Kandpal, N. Gupta, Study of structural and electrical properties of ZnO thin film for thin film transistor (TFT) applications. J. Mater. Sci.: Mater. Electron. **28**(21), 16013–16020 (2017)
9. S.F. Tseng, Investigation of post-annealing aluminum-doped zinc oxide (AZO) thin films by a graphene-based heater. Appl. Surf. Sci. **448**, 163–167 (2018)
10. L. Wen, B.B. Sahu, H.R. Kim et al., Study on the electrical, optical, structural, and morphological properties of highly transparent and conductive AZO thin films prepared near room temperature. Appl. Surf. Sci. **473**, 649–656 (2019)
11. X. Fenglin, M. Kaibo, B. Xuecheng et al., Characteraction of Ag-doped ZnO thin film synthesized by sol–gel method and its using in thin film solar cells. Optik–Int. J. Light Electron Optics **124**, 4876–4879 (2013)
12. J.Y. Lin, K.D. Zhong, P.T. Lee, Plasmonic behaviors of metallic AZO thin film and AZO nanodisk array. Opt. Exp. **24**(5), 5125–5135 (2016)
13. N.E. Duygulu, A.O. Kodolbas, A. Ekerim, Effects of argon pressure and rf power on magnetron sputtered aluminum doped ZnO thin films. J. Cryst. Growth **394**, 116–125 (2014)
14. H.R. Kim, J.B. Kim, Y.S. Choi et al., Deposition of AZO thin film using RF and ICP at facing magnetron sputtering system. Surf. Coat. Technol. **259**, 39–43 (2014)
15. X. Du, J. Li, X. Bi, The role of Ga partial substitution for Al in the enhanced conductivity of transparent AZO thin film. J. Alloys Compd. **698**, 128–132 (2017)
16. N. Witit-Anun, J. Kaewkhao, S. Chaiyakun, Effect of sputtering power on structural and optical properties of ALN thin film deposited by reactive DC sputtering technique. Adv. Mater. Res. **770**, 177–180 (2013)
17. H. Han, Y. Wang, Sh. Zhang et al., Influence of sputtering power on properties of ZnO thin films fabricated by RF sputtering in room temperature. Sci. China Inf. Sci. **55**, 951–955 (2011)
18. U. Helmersson, M. Lattemann, J. Bohlmark et al., Ionized physical vapor deposition (IPVD): a review of technology and applications. Thin Solid Films **513**(1–2), 1–24 (2006)
19. X. Wang, Z. Hu, X. Chen, X et al., Preparation of carbon nanotubes and nano-particles by microwave plasma-enhanced chemical vapor deposition. Scripta materialia, **44**(8–9), 1567–1570 (2001)
20. D. Acharyya, P. Bhattacharyya, An efficient BTX sensor based on ZnO nanoflowers grown by CBD method. Solid-State Electron **106**, 18–26 (2015)
21. M.R. Islam, M. Rahman, S.F.U. Farhad et al., Structural, optical and photocatalysis properties of sol–gel deposited Al-doped ZnO thin films. Surf. Interfaces **16**, 120–126 (2019)
22. S.R. Yousefi, D. Ghanbari, M. Salavati-Niasari et al., Photodegradation of organic dyes: simple chemical synthesis of Ni (OH) 2 nanoparticles, Ni/Ni (OH) 2 and Ni/NiO magnetic nanocomposites. J. Mater. Sci.: Mater. Electron. **27**(2), 1244–1253 (2016)
23. S. Ţălu, C. Luna, A. Ahmadpourian et al., J. Mater. Sci.: Mater. Electron. **27**, 11425–21143 (2019)
24. M. Molamohammadi, A. Arman, A. Achour et al., Microstructure and optical properties of cobalt–carbon

nanocomposites prepared by RF-sputtering. J. Mater. Sci.: Mater. Electron. **26**(8), 5964–5969 (2015)
25. M. Molamohammadi, C. Luna, A. Arman et al., Preparation and magnetoresistance behavior of nickel nanoparticles embedded in hydrogenated carbon film. J. Mater. Sci.: Mater. Electron. **26**(9), 6814–6818 (2015)
26. N. Ghobadi, Derivation of ineffective thickness method for investigation of the exact behavior of the optical transitions in nanostructured thin films. J. Mater. Sci.: Mater. Electron. **27**(9), 8951–8956 (2016)
27. A.K. Zak, W.A. Majid, M.E. Abrishami et al., X-ray analysis of ZnO nanoparticles by Williamson-Hall and size–strain plot methods. Solid State Sci. **13**(1), 251–256 (2011)
28. S. Ţălu, Ş Stach, V. Sueiras et al., Fractal analysis of AFM images of the surface of Bowman's membrane of the human cornea. Ann. Biomed. Eng. **43**(4), 906–916 (2015)
29. A. Zendehnam, S. Miri, Surface statistical properties of ZnO thin films produced by magnetron sputtering at different rates. Sci. Iran **20**(3), 1071–1075 (2013)
30. K.K. Manesh, B. Ramamoorthy, M. Singaperumal, Numerical generation of anisotropic 3D non-Gaussian engineering surfaces with specified 3D surface roughness parameters. Wear **268**(11–12), 1371–1379 (2010)
31. D.K. Kim, H.B. Kim, Room temperature deposition of Al-doped ZnO thin films on glass by RF magnetron sputtering under different Ar gas pressure. J. Alloys Compd. **509**(2), 421–425 (2011)
32. M. Shiravand, N. Ghobadi, E. Gholami Hatam, Influence of Ar gas pressure on the structural and optical properties and surface topography of Al-doped ZnO thin films sputtered by DC-magnetron sputtering method. Opt. Quantum Electron. **54**(12), 1–21 (2020)
33. T.H. Chen, T.C. Cheng, Z.R. Hu, The electrical and optical properties of AZO thin film under different post-annealing temperatures. Microsyst. Technol. **19**, 1787–1790 (2013)
34. D.J. Edison, W. Nirmala, K.D.A. Kumar et al., Structural, optical and nonlinear optical studies of AZO thin film prepared by SILAR method for electro-optic applications. Physica B **523**, 31–38 (2017)
35. N. Ghobadi, M. Shiravand, E. Gholami Hatam, Influence of sputtered time on the structural and optical characterization of Al-doped ZnO thin films prepared by RF sputtering technique. Opti. Quantum Electron. **53**(1), 1–13 (2021)
36. M.S. Bashar, R. Matin, M. Sultana et al., Effect of rapid thermal annealing on structural and optical properties of ZnO thin films fabricated by RF magnetron sputtering technique. J. Theor. Appl. Phys. **14**, 53–68 (2020)
37. N. Rahimi, V. Dalouji, A. Souri, Studying the optical density, topography, and structural properties of CZO and CAZO thin films at different annealing temperatures. Adv. Ceram. Progress **6**(2), 17–23 (2020)
38. K.D.A. Kumar, S. Valanarasu, S.R. Rosario et al., Evaluation of the structural, optical and electrical properties of AZO thin films prepared by chemical bath deposition for optoelectronics. Solid State Sci. **78**, 58–68 (2018)
39. A.Q. Abdullah, Surface and volume energy loss, optical conductivity of rhodamine 6G dye (R6G). Chem. Mater. Res. **3**(10), 1–9 (2013)
40. V. Dimitrov, S. Sakka, Electronic oxide polarizability and optical basicity of simple oxides. J. Appl. Phys. **79**(3), 1736–1740 (1996)

Publisher's Note Springer Nature remains neutral with regard to jurisdictional claims in published maps and institutional affiliations.

Springer Nature or its licensor (e.g. a society or other partner) holds exclusive rights to this article under a publishing agreement with the author(s) or other rightsholder(s); author self-archiving of the accepted manuscript version of this article is solely governed by the terms of such publishing agreement and applicable law.